

Highly tunable hot-electron distributions from scattering-mediated absorption

Jason Codrington[†], Noor Eldabagh[†], Kimberly Fernando[†], and Jonathan J. Foley IV^{*}

*Department of Chemistry, William Paterson University, 300 Pompton Road, Wayne, NJ,
07470, USA*

E-mail: foleyj10@wpunj.edu

^{*}To whom correspondence should be addressed

Abstract

Light-initiated generation of energetic carriers has attracted considerable attention as a paradigm for photocatalysis and solar energy conversion, and the use of noble metal nanoparticles that support localized surface plasmon resonances has been widely explored as a medium for realizing this paradigm. It was recently shown that composite nanostructures that enable the interplay between dielectric scattering resonances and broad-band absorption in small metal nanostructures, a phenomenon termed scattering-mediated absorption, can be used to mediate energetic carrier transfer and selective photochemistry with low-intensity light while completely circumventing plasmon resonance. In this work, we develop a multi-scale modeling approach for elucidating the hot-carrier dynamics initiated by scattering mediated absorption. Our calculations reveal that unique hot carrier distributions and dynamics arise from scattering mediated absorption as compared plasmon excitation, and also suggest that in a variety of circumstances, scattering mediated absorption may lead to more efficiency hot carrier generation than plasmon resonance under the same external illumination conditions. These results are an important first step in understanding the phenomena of scattering mediate hot carrier generation, which has potential for expanding the palette of materials that can be utilized for hot-carrier mediated photochemistry, and for enabling unique pathways for photocatalytic transformations.

Graphical TOC Entry

Some journals require a graphical entry for the Table of Contents. This should be laid out "print ready" so that the sizing of the text is correct. Inside the tocentry environment, the font used is Helvetica 8 pt, as required by *Journal of the American Chemical Society*. The surrounding frame is 9 cm by 3.5 cm, which is the maximum permitted for *Journal of the American Chemical Society* graphical table of content entries. The box will not resize if the content is too big: instead it will overflow the edge of the box. This box and the associated title will always be printed on a separate page at the end of the document.

Introduction

Various strategies that exploit the optical properties of metal nanoparticles, namely their ability to support localized surface plasmons resonances (LSPR, which are collective oscillations of their conduction electrons driven by visible light), have been explored recently with the aim of using low-intensity light to efficiently drive chemical reactions.¹⁻⁴ The interest in this area has been motivated partly by the fact that metal nanoparticles (most prominently silver and gold) are exceptionally good absorbers of visible light, so they are ideal candidates for harvesting solar photons.⁵ Importantly, the resonant properties of plasmonic particles are highly tunable by parameters under synthetic control such as geometry, composition, surface chemistry, and the surrounding environment.⁶⁻⁸ An emerging paradigm that exploits LSPR for photocatalysis is known as Plasmon-mediated Hot-Electron Transfer (PHET), and a growing number of reports are demonstrating the ability of PHET to catalyze energetically demanding chemical reactions.⁹⁻¹⁶ In PHET, the collective plasmon excitation decays rapidly (on a 10 femtosecond timescale) to a non-equilibrium distribution of energetic electron-hole pairs, or a so-called hot-electron distribution^{2,17-21} Hot-electrons can deposit energy into reactive degrees of freedom of molecules adsorbed to the nanoparticle surface, thereby initiating chemical transformations. Despite the considerable progress made in demonstrating the potential of the paradigm of PHET, its widespread application faces several challenges. The intrinsic optical properties of noble metals that give rise to the extraordinarily large absorption cross sections associated with LSPR are also fundamentally related to the broad energy spectra and short lifetimes associated with LSPR and the subsequent hot-electron distributions.²² Furthermore, the timescale of hot-electron relaxation competes with transfer to adsorbate states (both occur on 100 fs timescales), which fundamentally limits the efficiency of energy transfer.¹⁹ Finally, the most promising plasmonic materials typically have poor catalytic activity, and similarly, good catalytic metals typically are poor light harvesters.¹⁵

Considering this, an incredible opportunity exists to identify new classes of structures for mediating light-matter interactions and energy transfer events that offer the same ad-

vantages as metal nanoparticles, namely exceptional light-harvesting potential, while also offering greater selectivity and efficiency in energy transfer, as well as tunable surface chemistry for enhanced catalytic activity. Ideally, such structures could be made mostly, if not entirely, from cost-effective materials. Recent progress towards this aim has been made by designing hybrid nanostructures that effectively delegate the light-harvesting and catalytic functions to separate components of the structure. Recently, Halas and co-workers demonstrated an antenna-reactor concept that leverages the near-field enhancement from aluminum plasmons to generate energetic carriers on palladium islands and showed the efficacy of this strategy for the photocatalytic transformation of acetylene to ethylene.¹⁵ Two of the current authors, along with Sun and co-workers, demonstrated a phenomena known as scattering-mediated absorption where dielectric scattering resonances in SiO_2 ionospheres were utilized to induce resonant absorption in non-plasmonic platinum nanoparticles in SiO_2/Pt nanohybrids.¹³ The scattering-mediated absorption (SMA) phenomena was also observed to induce highly selective photocatalytic oxidation of benzyl alcohol to benzaldehyde.¹³ Zhang *et al.* independently described a SMA phenomenon in Au-TiO_2 nanohybrids that leveraged so-called whispering gallery modes to enhance plasmonic and non-plasmonic absorption in gold nanoparticles, and demonstrated these structures efficacy for photocatalytic water splitting.¹⁴ Interestingly, hot-carrier transfer was implicated in the photocatalytic mechanisms that resulted from these SMA phenomena.^{13,14} The prospect of using SMA in hybrid dielectric/metal nanostructures to initiate hot-carrier generation and transfer is particularly compelling as it could completely circumvent plasmon excitation. Not only does this open up possibilities to utilize a broader palette of materials, it also presents the possibility of realizing unique photocatalytic pathways owing to differences in the distributions and dynamics of energetic carriers produced by SMA compared to those produced by plasmon excitation.

The push to identify novel structures for mediating hot-carrier generation and transfer has been paralleled by efforts to develop theoretical methodologies to elucidate these processes. The underlying electronic structure has been treated both within free-electron models

confined by potential wells^{17,23–26} (here called “particle-in-a-well” (PIW) models), as well as by *ab initio* approaches.^{18,20,21,27} Using PIW models, Govorov and co-workers developed a theory of hot-electron generation within the framework of time-dependent perturbation theory that has elucidated a variety of shape- and size-dependent factors for optimizing the hot-carrier generation.^{17,23} A similar approach was also pursued by Kumarasinghe *et al.* suggesting that nanorods are exceptionally good structures for hot-carrier generation.²⁵ García de Abajo and co-workers recently described a quantum master equation approach with an underlying PIW model that elucidated a number of key factors that influence hot-carrier excitation and decay dynamics.²⁶ The utilization of *ab initio* approaches by Sundararaman *et al* has also provided valuable insights into the role that a metals band-structure plays in determining the efficiency of hot-carrier generation, and particularly in the asymmetry between hot-electron and hot-hole generation.¹⁸ Nordlander and co-workers have directly compared free-electron and *ab initio* approaches and found negligible impact on hot-carrier generation and dynamics in Ag nanospheres resulting from electron correlation,²⁴ though Bernardi *et al* have demonstrated that many-body effects are important in the hot-carrier dynamics resulting from surface plasmon polaritons in gold and silver.²⁷

We develop an novel approach for studying hot-carrier dynamics that may arise from arbitrary electromagnetic fields, including the unique near-fields that arise from SMA on hybrid dielectric-metal nanoparticles and plasmon resonance on noble metal nanoparticles. We consider the electronic degrees of freedom on the metal nanoparticle subject to the time-dependent Hamiltonian

$$\hat{H}(t) = \hat{H}_{el} - \mathbf{E}(t) \cdot \hat{\boldsymbol{\mu}}, \quad (1)$$

where the specific form of $\mathbf{E}(t)$ derives from a rigorous time-domain electrodynamics calculation with a realistic model of the nanostructures in question and \hat{H}_{el} describes non-interacting electrons confined by an infinite potential well. Through appropriate choice of the shape of the potential well, nanocubes and nanospheres are modeled. We compute the time-domain field using a commercial simulator based on the finite-difference time-domain method;²⁸ more

details are given in the supplemental information.

The many-electron wavefunction of the metal nanoparticles is expanded in terms of a configuration-interaction expansion that includes all singly-excited configurations,

$$|\Psi_{CIS}\rangle = c_0|\Phi_0\rangle + \sum_{i,a} c_i^a |\Phi_i^a\rangle, \quad (2)$$

where the configuration $|\Phi_i^a\rangle$ has an electron excited from orbital i to orbital a , and c_0 and c_i^a are complex expansion coefficients. Unless otherwise specified, indices i, j will indicate orbitals which are occupied in the ground state reference configuration and indices a, b will indicate orbitals which are unoccupied in the ground state reference.

The time-evolution of the wavefunction can be subsumed in the expansion coefficients, which allows the TDSE to be written

$$i\hbar \frac{d}{dt} \mathbf{c}(t) = \mathbf{H}(t) \mathbf{c}(t) \quad (3)$$

where $\mathbf{c}(t)$ is the vector of complex expansion coefficients and $\mathbf{H}(t)$ is the time-dependent Hamiltonian matrix. The Hamiltonian matrix is comprised of three unique blocks in the CIS model,

$$\mathbf{H}(t) = \begin{pmatrix} \langle \Phi_0 | \hat{H}(t) | \Phi_0 \rangle & \langle \Phi_0 | \hat{H}(t) | \Phi_i^a \rangle \\ \langle \Phi_j^b | \hat{H}(t) | \Phi_0 \rangle & \langle \Phi_j^b | \hat{H}(t) | \Phi_i^a \rangle \end{pmatrix}. \quad (4)$$

Explicit expressions for Hamiltonian matrix elements are given for both the nanocube and nanosphere models in the supplemental information. Given the simplicity of the underlying electronic Hamiltonian, the field-free Hamiltonian matrix is diagonal, and only the dipolar interaction of the nanoparticle with the external field can induce transitions among the electronic configurations, hence the treatment in this work neglects excited-state decay contributions from electron-electron scattering. These contributions will be explored in future work. Also because of the diagonal nature of field-free Hamiltonian, each configuration $|\Phi_i^a\rangle$ is an eigenfunction of the field-free Hamiltonian. This simplifies the interpretation of the

electronic structure relative to the CIS wavefunction in molecular quantum mechanics where electron repulsion is included in the Hamiltonian and the excited electronic eigenfunctions are linear combinations of singly-excited configurations. The multiplication of the Hamiltonian matrix on the coefficient vector generates the gradient of the coefficient vector in time, and a variety of algorithms are known that use this information to propagate the wavefunction in time. Here we use a symplectic integrator described in Ref. 29.

We analyze the hot-carrier distribution and dynamics that results from SMA and plasmon excitation by computing the instantaneous populations of orbitals both above and below the Fermi level of the metal nanostructure. In our model, the orbitals are energy eigenstates of a 1-electron Hamiltonian and have well-defined kinetic energy, and the orbital populations are given by the diagonal elements of the 1-electron reduced density matrix,

$$^1D_q^q(t) = \langle \Psi(t) | \hat{a}_q^\dagger \hat{a}_q | \Psi(t) \rangle, \quad (5)$$

where the second-quantized operator \hat{a}_q^\dagger (\hat{a}_q) creates (kills) an electron in orbital q . The orbital indices can be uniquely mapped to the relevant orbital quantum numbers (n_x, n_y, n_z for the nanocube model, n, l, m for the nanosphere model) so that the orbital energies can be readily computed.

Our model of the Au nanocube has a number of dipole-allowed transitions between 1.3 and 3.3 eV, and the Au LSPR has partial overlap with a transition at approximately 2.5 eV (see Figure 1a). The spectral flexibility of dielectric scattering resonances allows them to be tuned to overlap with one or more of these transition energies; for example, a $d = 270nm$ TiO₂ NS has a scattering resonance that overlaps with an Au transition at 3.1 eV, and a $d = 685nm$ TiO₂ NS has scattering resonances that overlap with every transition between 1.3 and 3.3 eV. As proxies of the hot-carrier dynamics, we plot the population dynamics of the highest and lowest energy orbitals in our active space, which lie 2.2 eV above and 1.6 eV below the Fermi energy, respectively (Figure 1 (a) and (b)). Snapshots of the populations

of all active orbitals at various times are also provided in the supplemental information. We observe that LSPR the LSPR generates a relatively small population of hot-carriers and hot-hole generation with field-driven dynamics that evolve on a short (10 fs) timescale.

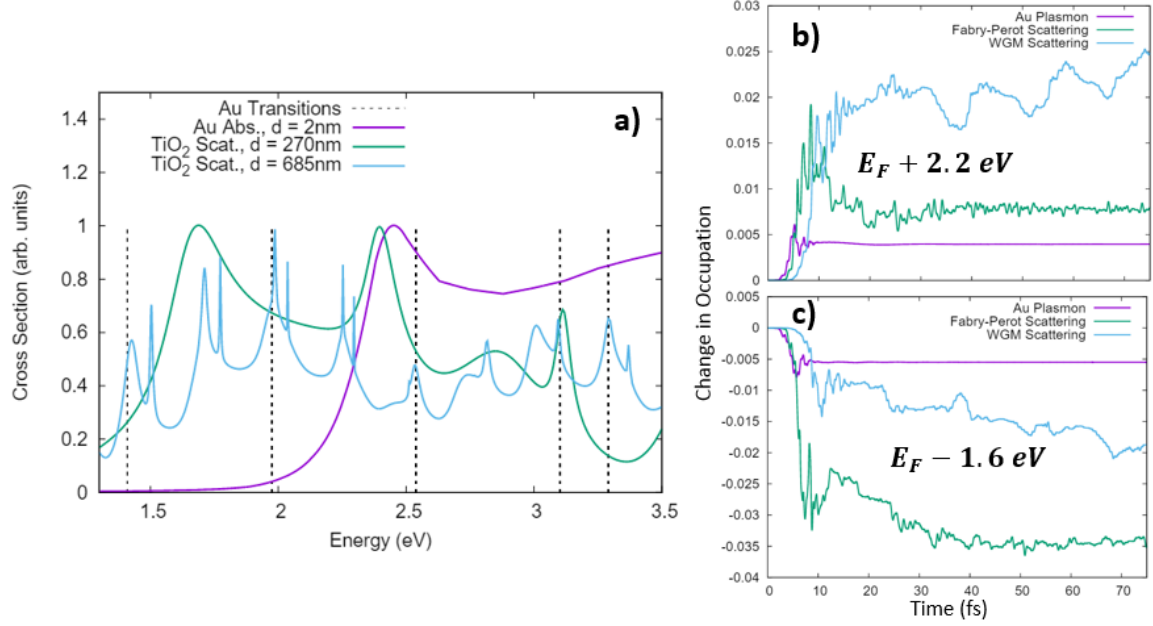


Figure 1: Three regimes for light-matter interactions leading to unique spatial and temporal shaping of the incident field, and the corresponding impact on electronic dynamics in a Au nanocube. Panel (a) shows the absorption of a 2nm gold nanocube and the scattering of 270 nm and 685 nm TiO₂ nanospheres that display predominately Fabry-Perot and Whispering Gallery Mode visible resonances, respectively. These spectra are overlaid with the dipole-allowed transitions in our quantum mechanical Au NC model. Both dielectric scattering resonances show more efficient generation of hot-electrons (Panel (b)) and hot-holes (Panel (c)) compared to LSPR in this case.

Methods

Electronic structure of metal nanospheres

For spherical metal nanoparticles, we approximate the one-electron orbitals as energy eigenstates of the particle-in-a-spherical-well. For a particle confined by a spherical well with radius R , the potential is 0 when $r < R$ and infinity with $r \geq R$, so that only kinetic energy

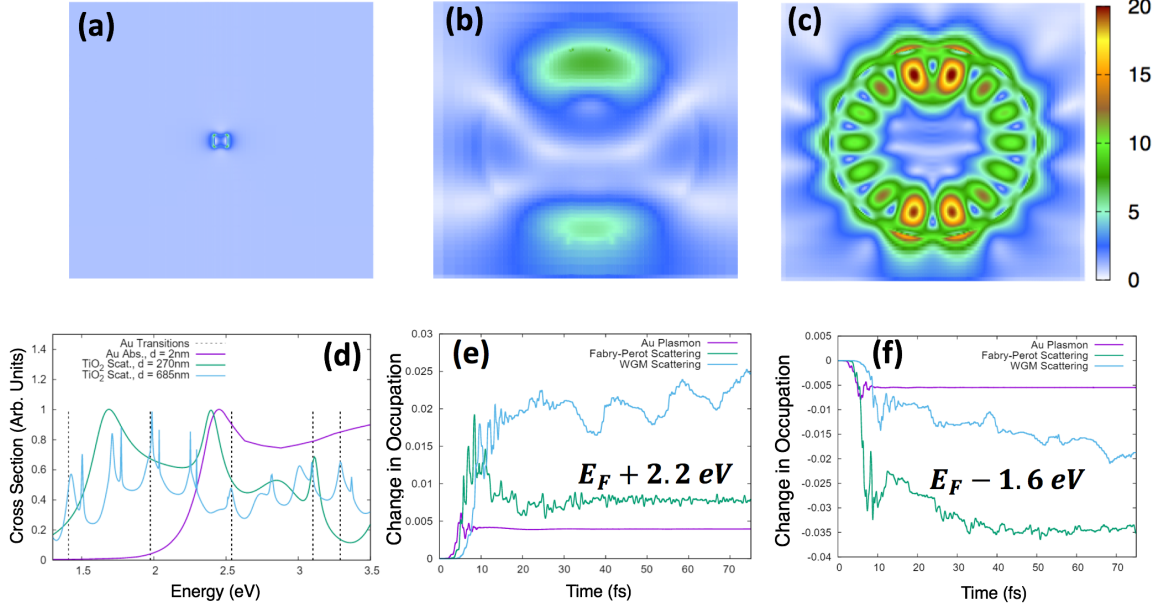


Figure 2: Three regimes for light-matter interactions leading to unique spatial and temporal shaping of the incident field, and the corresponding impact on electronic dynamics in a Au nanocube. Panel (a) shows the absorption of a 2nm gold nanocube and the scattering of 270 nm and 685 nm TiO₂ nanospheres that display predominately Fabry-Perot and Whispering Gallery Mode visible resonances, respectively. These spectra are overlaid with the dipole-allowed transitions in our quantum mechanical Au NC model. Both dielectric scattering resonances show more efficient generation of hot-electrons (Panel (b)) and hot-holes (Panel (c)) compared to LSPR in this case.

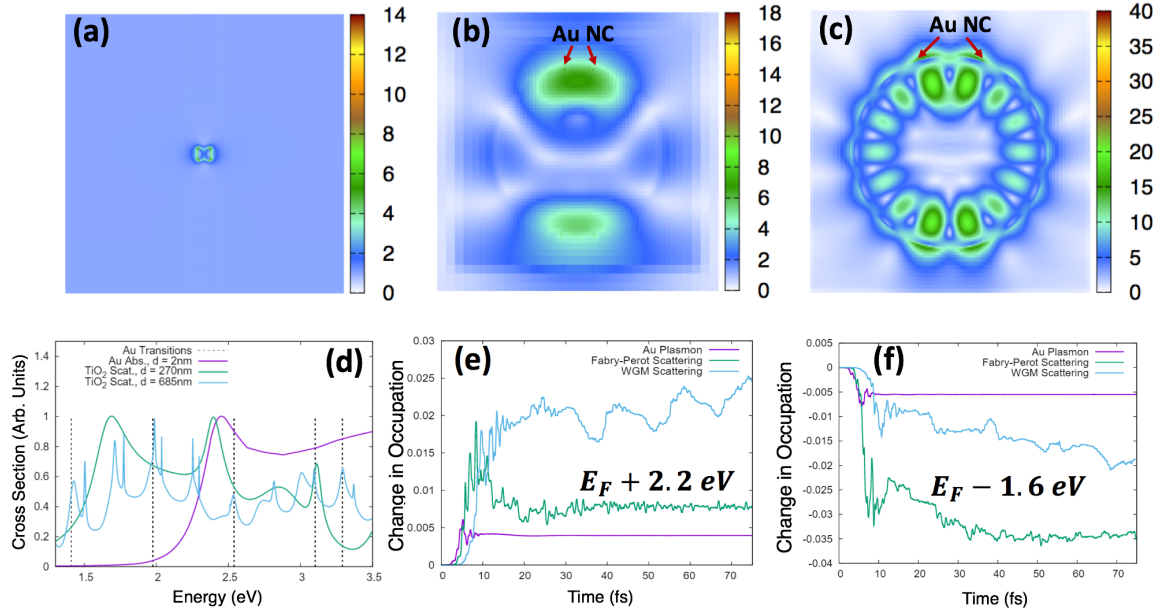


Figure 3: Three regimes for light-matter interactions leading to unique spatial and temporal shaping of the incident field, and the corresponding impact on electronic dynamics in a Au nanocube. Panel (a) shows the absorption of a 2nm gold nanocube and the scattering of 270 nm and 685 nm TiO_2 nanospheres that display predominately Fabry-Perot and Whispering Gallery Mode visible resonances, respectively. These spectra are overlaid with the dipole-allowed transitions in our quantum mechanical Au NC model. Both dielectric scattering resonances show more efficient generation of hot-electrons (Panel (b)) and hot-holes (Panel (c)) compared to LSPR in this case.

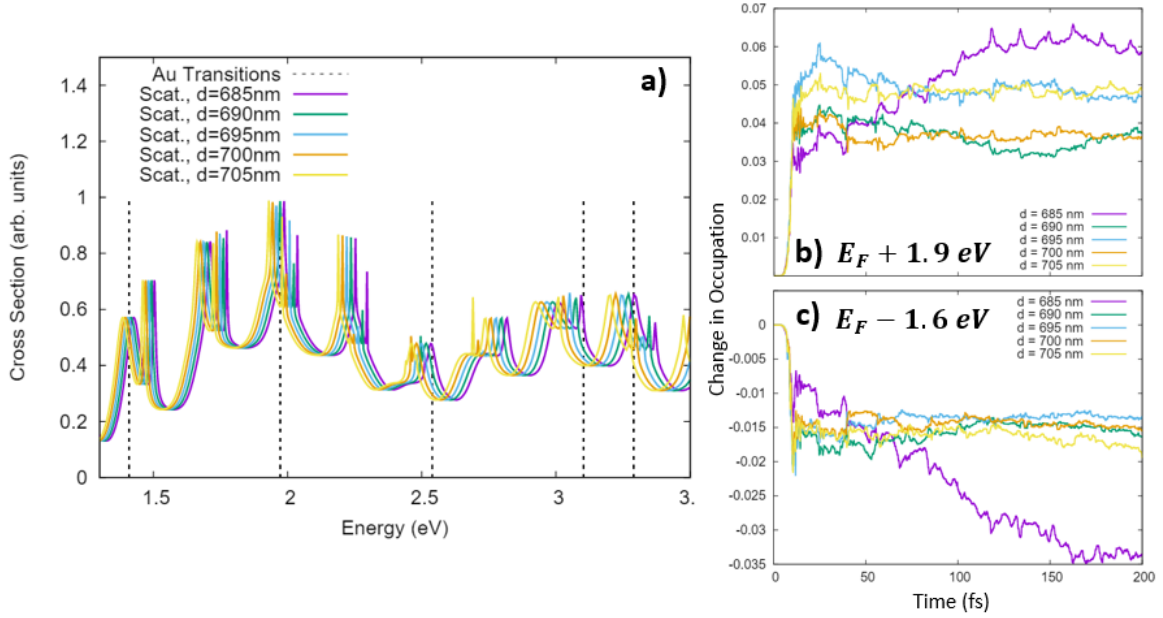


Figure 4: Fine-shaping of the spatial and temporal shaping of the incident field through the geometry of the dielectric nanosphere. Panel (b) shows the scattering spectra of a size progression of TiO_2 nanospheres that display predominately Whispering Gallery Mode visible resonances. The 685nm nanosphere's scattering spectra has the best overlap with the dipole-allowed transitions in the Au NC model, and this structure shows most efficient generation of hot-electrons in the most energetic orbitals included in our active space (Panel (b)), and more efficiently generation of hot holes in the lowest energy orbitals included in our active space (Panel (c)).

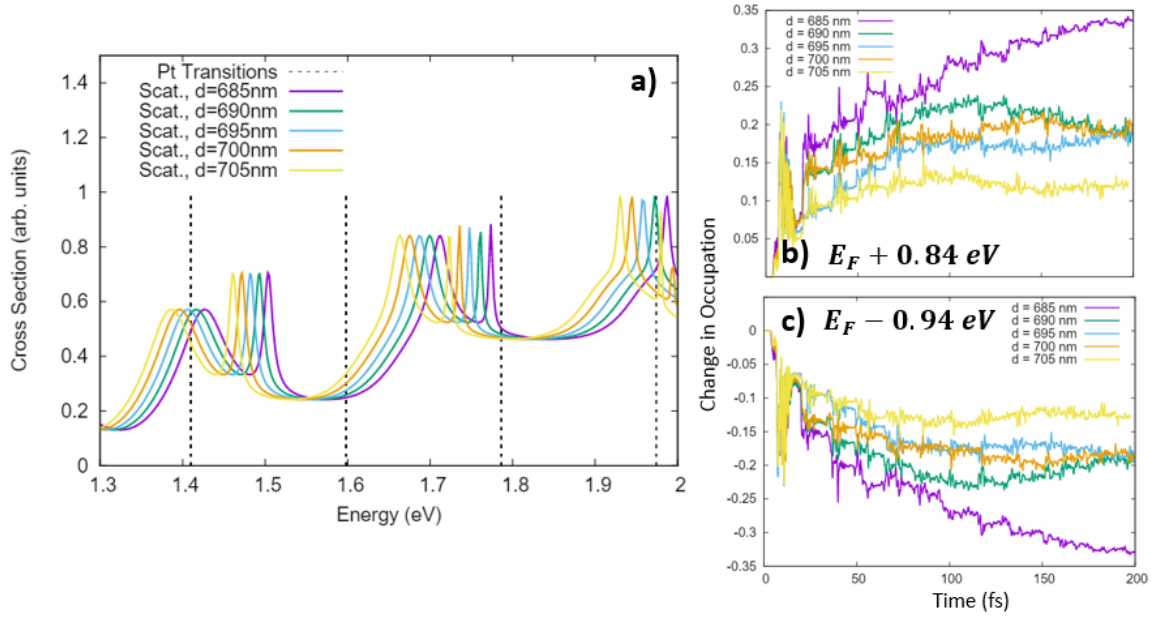


Figure 5: Progressive scattering spectra of TiO_2 nanospheres overlaid with the dipole-allowed transitions of the Pt NC Model show partial overlap between the resonances of the 685 nm, 690 nm, and 695 nm nanospheres (Panel (a)). The 685 nm nanosphere's scattering again shows greatest efficacy for generating hot-electrons in the most energetic orbitals and hot-holes in the lowest energy orbitals in our Pt NC model.

contributes to the energetic. The energy eigenstates have the form^{22,30}

$$\psi_{n,l,m}(r, \theta, \phi) = j_l(\alpha r) Y_{l,m}(\theta, \phi), \quad (6)$$

where $j_l(\alpha r)$ are the spherical Bessel functions and $Y_{l,m}(\theta, \phi)$ are the spherical Harmonics. In our numerical implementation, we use the asymptotic approximation of the spherical Bessel functions $j_l(\alpha r) \approx \cos(\alpha r - \frac{\pi}{2}(l+1))/r$. To evaluate the spherical harmonics, we use a recursive algorithm described in Ref. 31 to evaluate the associated Legendre polynomials. The energy eigenfunctions must vanish at $r = R$, which leads to the following form for the one-electron orbitals:

$$\psi_{n,l,m}(r, \theta, \phi) = \frac{2}{\sqrt{R}} \frac{\cos\left(\frac{\pi}{2}(2n+2+l)\frac{r}{R} - \frac{\pi}{2}(l+1)\right)}{r} Y_{l,m}(\theta, \phi). \quad (7)$$

The energy eigenvalues have the form

$$E_{n,l} = \frac{\hbar^2 \pi^2}{8mR^2} (2n+l+2)^2. \quad (8)$$

From the definition of the spherical polar coordinates, the x , y , and z components of the transition dipole integrals have the form

$$\langle \mu_x \rangle = \int_0^R \int_0^{2\pi} \int_0^\pi \psi_{n,l,m}^* \hat{\mu}_x \psi_{n',l',m'} r^2 \sin\theta \, dr \, d\theta \, d\phi \quad (9)$$

$$\langle \mu_y \rangle = \int_0^R \int_0^{2\pi} \int_0^\pi \psi_{n,l,m}^* \hat{\mu}_y \psi_{n',l',m'} r^2 \sin\theta \, dr \, d\theta \, d\phi \quad (10)$$

$$\langle \mu_z \rangle = \int_0^R \int_0^{2\pi} \int_0^\pi \psi_{n,l,m}^* \hat{\mu}_z \psi_{n',l',m'} r^2 \sin\theta \, dr \, d\theta \, d\phi, \quad (11)$$

where $\hat{\mu}_x = -e \cdot r \cdot \sin\theta \cos\phi$, $\hat{\mu}_y = -e \cdot r \cdot \sin\theta \sin\phi$, $\hat{\mu}_z = -e \cdot r \cdot \cos\theta$, and e is the charge of the electron.

In this work, we neglect the x and y components of the field and evaluate μ_z numerically,

where the integral can be simplified to

$$\langle \mu_z \rangle = \delta_{m,m'} \cdot 2\pi \cdot \int_0^R \int_0^{2\pi} j_{n,l}(\alpha r) P_{n,l}(\cos \theta) \hat{\mu}_z j_{n',l'}(\alpha r) P_{n',l'}(\cos \theta) r^2 \sin \theta dr d\theta, \quad (12)$$

where $j_{n,l}(\alpha r)$ denotes the asymptotic approximation to the Spherical Bessel Function (written explicitly in Eq.) and $P_{n,l}(\cos \theta)$ denotes the associated Legendre polynomial.

Electronic structure of metal nanocubes

For cubic metal nanoparticles, we approximate the one-electron orbitals as energy eigenstates of the particle-in-a-cubic-well. For a particle confined by a cubic well with length L , the potential is 0 when $x < L, y < L, z < L$ and infinity otherwise. The energy eigenstates have the form

$$\psi_{nx,ny,nz} = \left(\frac{2}{L}\right)^{3/2} \sin\left(\frac{n_x \pi x}{L}\right) \sin\left(\frac{n_y \pi y}{L}\right) \sin\left(\frac{n_z \pi z}{L}\right). \quad (13)$$

The energy eigenvalues have the form

$$E_{nx,ny,nz} = \frac{\hbar^2 \pi^2}{2 m L^2} (n_x^2 + n_y^2 + n_z^2). \quad (14)$$

The transition dipole integrals can be evaluated analytically,

$$\begin{aligned} \langle \psi_{nx,ny,nz} | \hat{\mu}_x | \psi_{n'_x,n'_y,n'_z} \rangle &= e \delta_{ny,ny'} \delta_{nz,nz'} \frac{L(\pi(n_x - n'_x)\sin(\pi(n_x - n'_x)) + \cos(\pi(n_x - n'_x)) - 1)}{\pi^2(n_x - n'_x)^2} \\ &\quad - e \delta_{ny,ny'} \delta_{nz,nz'} \frac{L(\pi(n_x + n'_x)\sin(\pi(n_x + n'_x)) + \cos(\pi(n_x + n'_x)) - 1)}{\pi^2(n_x + n'_x)^2} \end{aligned}$$

Finite-difference time-domain calculations

A commercial simulator based on the finite-difference time-domain method²⁸ was used to compute the electric field, $E(t)$ 1 Å away from the nanoparticle surface in each of the scenarios considered. The displacement was taken along the z -axis, corresponding to the polarization direction of incident light since the strongest near-field enhancement is expected along this

direction. A grid spacing of 1 Å in $x, y, \text{ and } z$ was utilized in a cubic region extending 1 nm beyond the metal NP surface, and a non-uniform mesh was utilized otherwise with $dx, dy, dz \leq 20 \text{ nm}$. For each composite structure, a nanoparticle was placed at the surface of the dielectric nanosphere at an angle of 20° with respect to the propagation axis of the incident light. In all simulations, light propagates along the x axis and is polarized along the z axis. The metal nanoparticles are centered at $y = 0$. A total-field scattered-field source was used to illuminate the structures. The FDTD simulations were terminated when the ratio of the total energy in the simulation volume to the total energy injected by the illumination source falls below $1e - 6$. Because the WGMs are higher quality factor resonances, longer time is typically required for these simulations are compared to the plasmonic particles alone.

The resulting time-domain fields were fed into our TDCIS code, allowing us to simulate the electronic dynamics driven by rigorously-computed nearfields from scattering and plasmon resonances, which show strong spatiotemporal modification relative to freely propagating light. The electric field was scaled by a factor $E_0 \approx 614,000,000 \text{ V/m}$ so that the peak power of the illumination source is $1e15 \text{ W/m}^2$. The electric field was sampled at intervals of approximately 0.0028 fs for all simulations, which leads to a time-step that ensures stability of the wavefunction propagation with the relevant energy scales of our simulations. Our wavefunction propagation scheme requires the evaluation of the electric field at intermediate times between these timesteps, and we use a simple update scheme based on centered-finite differences to approximate the electric fields at these times. As an example, if the electric field is known at times $t_1, t_2 = t_1 + dt$, and $t_3 = t_1 + 2 \cdot dt$ where $dt = 0.0028$, and knowledge of the field is required at some time $t_m = t_2 + m \cdot dt$ where m is non-integer, $E(t_m)$ is estimated as follows:

$$\mathbf{E}(t_m) = \mathbf{E}(t_2) + \frac{\mathbf{E}(t_3) - \mathbf{E}(t_1)}{t_3 - t_1} \cdot m \cdot dt. \quad (15)$$

The permittivity for Au comes from the data set by Johnson and Christy,³² and the permittivity for Pt comes from the data set by Palik.³³ We assume a static dielectric constant of 2.6 for TiO_2 in this work, and neglect its UV absorption.

Acknowledgment

This work was performed, in part, utilizing resources at the Center for Nanoscale Materials, a US Department of Energy, Office of Science, Office of Basic Energy Sciences User Facility (contract no. DE-AC02-06CH11357). JJF Acknowledges the College of Science and Health for startup support. J.C. and N.E. acknowledge the NSF-GS-LSAMP for support. K.F. acknowledges the WPU CFR for support. [†]J.C., N.E., and K.F. contributed equally to this work.

References

- (1) Linic, S.; Christopher, P.; Ingram, D. B. Plasmonic-metal nanostructures for efficient conversion of solar to chemical energy. *Nat. Mater.* **2011**, *10*, 911921.
- (2) Kale, M. J.; Avanesian, T.; Christopher, P. Direct Photocatalysis by Plasmonic Nanostructures. *ACS Catalysis* **2013**, *4*, 116–128.
- (3) Zhou, N.; López-Puente, V.; Wang, Q.; Polavarapu, L.; Pastoriza-Santos, I.; Xu, Q.-H. Plasmon-enhanced light harvesting: applications in enhanced photocatalysis, photodynamic therapy and photovoltaics. *RSC Adv.* **2015**, *5*, 29076.
- (4) Park, J. Y.; Kim, S. M.; Lee, H.; Nedrygailov, I. I. Hot-electron-mediated surface chemistry: toward electronic control of catalytic activity. *Acc. Chem. Res.* **2015**, *48*, 2475.
- (5) Atwater, H. A.; Polman, A. Plasmonics for improved photovoltaic devices. *Nature Mater.* **2010**, *9*, 205–213.
- (6) Sun, Y.; Xia, Y. Shape-controlled synthesis of gold and silver nanoparticles. *Science* **2002**, *298*, 21762179.

- (7) Burda, C.; Chen, X.; Narayanan, R.; El-Sayed, M. A. Chemistry and properties of nanocrystals of different shapes. *Chem. Rev.* **2005**, *105*, 10251102.
- (8) Gramotnev, D. K.; Bozhevolnyi, S. I. Plasmonics beyond the diffraction limit. *Nature Photon.* **2010**, *4*, 8391.
- (9) Christopher, P.; Xin, H.; Linic, S. Visible-light-enhanced catalytic oxidation reactions on plasmonic silver nanostructures. *Nature Chem.* **2011**, *3*, 467472.
- (10) Marimuthu, A.; Zhang, J.; Linic, S. Tuning selectivity in propylene epoxidation by plasmon mediated photo-switching of Cu oxidation state. *Science* **2013**, *339*, 1590–1593.
- (11) Mukherjee, S.; Libisch, F.; Large, N.; Neumann, O.; Brown, L. V.; Cheng, J.; Lasater, J. B.; Carter, E. A.; Nordlander, P.; Halas, N. J. Hot Electrons Do the Impossible: Plasmon-Induced Dissociation of H₂ on Au. *Nano Letters* **2013**, *13*, 240–247.
- (12) Li, Z.; Foley IV, J. J.; Peng, S.; Sun, C.-J.; Ren, Y.; Wiederrecht, G. P.; Gray, S. K.; Sun, Y. Reversible Modulation of Surface Plasmons in Gold Nanoparticles Enabled by Surface Redox Chemistry. *Angew. Chem.* **2015**, *127*, 9076–9079.
- (13) Zhang, N.; Han, C.; Xu, Y.-J.; Foley IV, J. J.; Zhang, D.; Codrington, J.; Gray, S. K.; Sun, Y. Near-field dielectric scattering promotes optical absorption by platinum nanoparticles. *Nat. Photon.* **2016**, *10*, 473–482.
- (14) Zhang, J.; Jin, X.; Morales-Guzman, P. I.; Yu, X.; Liu, H.; Zhang, H.; Razzari, L.; Claverie, J. P. Engineering the Absorption and Field Enhancement Properties of Au-TiO₂ Nanohybrids via Whispering Gallery Mode Resonances for Photocatalytic Water Splitting. *ACS Nano* **2016**, *10*, 4496–4503.
- (15) Swearer, D. F.; Zhao, H.; Zhou, L.; Zhang, C.; Robatjazi, H.; Martirez, J. M. P.; Krauter, C. M.; Yazdi, S.; McClain, M. J.; Ringe, E. et al. Heterometallic antennare-

- actor complexes for photocatalysis. *Proceedings of the National Academy of Sciences* **2016**, *113*, 8916–8920.
- (16) Sousa-Castillo, A.; Comesaa-Hermo, M.; Rodriguez-Gonzalez, B.; Prez-Lorenzo, M.; Wang, Z.; Kong, X.-T.; Govorov, A. O.; Correa-Duarte, M. A. Boosting Hot Electron-Driven Photocatalysis through Anisotropic Plasmonic Nanoparticles with Hot Spots in AuTiO₂ Nanoarchitectures. *The Journal of Physical Chemistry C* **2016**, *120*, 11690–11699.
- (17) Govorov, A. O.; Zhang, J.; Gun'ko, Y. K. Theory of photoinjection of Hot Plasmonic Carriers from Metal Nanostructures into Semiconductors and Surface Molecules. *J. Phys. Chem. C* **2013**, *117*, 16616–16631.
- (18) Sundararaman, R.; Narang, P.; Jermyn, A. S.; Goddar III, W. A.; Atwater, H. A. Theoretical predictions for hot-carrier generation from surface plasmon decay. *Nat. Commun.* **2014**, *5*, 5788.
- (19) Wu, K.; Chen, J.; McBride, J. R.; Lian, T. Efficient hot-electron transfer by a plasmon-induced interfacial charge-transfer transition. *Science* **2015**, *349*, 632.
- (20) Ma, J.; Wang, Z.; Wang, L.-W. Interplay between plasmon and single-particle excitations in a metal nanocluster. *Nat. Commun.* **2015**, *6*, 10107.
- (21) Brown, A. M.; Sundararaman, R.; Narang, P.; Goddard III, W. A.; Atwater, H. A. Nonradiative Plasmon Decay and Hot Carrier Dynamics: Effects of Phonons, Surfaces, and Geometry. *ACS Nano* **2016**, *10*, 957–966.
- (22) Kraus, W. A.; Schatz, G. C. Plasmon resonance broadening in small metal particles. *J. Chem. Phys.* **1983**, *79*, 61306139.
- (23) Zhang, H.; Govorov, A. O. Optical Generation of Hot Plasmonic Carriers in Metal

- Nanocrystals: The Effects of Shape and Field Enhancement. *J. Phys. Chem. C* **2014**, *118*, 7606–7614.
- (24) Manjavacas, A.; Liu, J. G.; Kulkarni, V.; Nordlander, P. Plasmon-Induced Hot Carriers in Metallic Nanoparticles. *ACS Nano* **2014**, *8*, 7630–7638.
- (25) Kumarasinghe, C. S.; Premaratne, M.; Bao, Q.; Agrawal, G. P. Theoretical analysis of hot electron dynamics in nanorods. *Sci. Rep* **2015**, *5*, 12140.
- (26) Saavedra, J. R. M.; Asenjo-Garcia, A.; García de Abajo, F. J. Hot-Electron Dynamics and Thermalization in Small Metallic Nanoparticles. *ACS Photonics* **2016**, *0*, null.
- (27) Bernardi, M.; Mustafa, J.; Neaton, J. B.; Louie, S. G. Theory and computation of hot carriers generated by surface plasmon polaritons in noble metals. *Nat. Commun.* **2015**, *6*, 7044.
- (28) Lumerical Solutions, Inc., <http://www.lumerical.com/tcad-products/mode/>.
- (29) Sanz-Serna, J. M.; Portillo, A. Classical numerical integrators for wave-packet dynamics. *J. Chem. Phys.* **1996**, *104*, 2349–2355.
- (30) Scholl, J. A.; Koh, A. L.; Dionne, J. A. Quantum plasmon resonances of individual metallic nanoparticles. *Nature* **2012**, *483*, 421–427.
- (31) Press, W. H.; Teukolsky, S. A.; Vetterling, W. T.; Flannery, B. P. *Numerical Recipes in C: The Art of Scientific Computing*, 2nd ed.; Cambridge University Press, 1992.
- (32) Johnson, P. B.; Christy, R. W. Optical constants of noble metals. *Phys. Rev. B* **1972**, *6*, 4370.
- (33) Palik, E. D. *Handbook of optical constants of solids*; Academic Press, 1998.